Lubrication of dislocation glide in forsterite by Mg vacancies: insights from Peierls-Nabarro modeling

Richard Skelton [a,*] and Andrew M. Walker[b]

[a] Research School of Earth Sciences, Australian National University, Canberra, ACT, 0200, Australia

(ORCID: 0000-0003-1583-2312)

[b] School of Earth and Environment, University of Leeds, Leeds, LS2 9JT, UK

(ORCID: 0000-0003-3121-3255)

* Corresponding author: richard.skelton@anu.edu.au

Abstract

Dislocation glide is an important contributor to the rheology of olivine under conditions of high stress and low to moderate temperature, such as occur in mantle wedges. Interactions between point defects and dislocation core may alter the Peierls stress, σ_p, and has been suggested that vacancy-related defects may selectively enhance glide on certain slip systems, changing the olivine deformation fabric. In this study, the Peierls-Nabarro model, parameterized by generalized stacking fault (GSF) energies calculated atomistically using empirical interatomic potentials, is used to determine the effect of bare Mg vacancies on the Peierls stresses of [100](010) and [001](010) dislocations in forsterite. Mg vacancies considerably reduce GSF energies and, consequently, σ_p for dislocations gliding on (010) in olivine. The magnitude of this decrease depends strongly on dislocation and the type of the lattice site, with vacant M2 sites producing the largest reduction of σ_p. The [001](010) slip system is found to be more sensitive than the [100](010) slip system to the presence of vacancies. Although, at ambient pressure, σ_p is lower for [100](010) than [001](010) edge dislocations, $d\sigma_p/dP$ is greater for [100](010) dislocations, resulting in a change in the preferred slip system at 1.5 GPa. By preferentially lubricating [001](010) glide, Mg vacancies reduce the pressure at which this cross-over occurs. An M2 vacancy

concentration at the glide plane of 0.125 defects/site is sufficient to reduce cross-over to 0.7 GPa. This may account for the existence of the B-type olivine deformation fabric in the corners of mantle wedges.

Keywords: Forsterite; dislocation; Peierls stress; cation vacancies; atomic-scale modeling

1. Introduction

Forsterite-rich olivine is the dominant component of the Earth's upper mantle, composing ~60-70% of its bulk by volume. Olivine is also the weakest major phase in this region of the Earth’s interior, and accordingly controls its rheology. Interpreting seismological models of the Earth's upper mantle in terms of the dynamics of plastic flow thus requires an intimate understanding of the atomic-scale mechanisms that contribute to the deformation of olivine. A number of mechanisms contribute to the rheology of olivine under mantle conditions, such as grain boundary diffusion (e.g. Mei and Kohlstedt 2000); grain boundary sliding, accommodated by either elastic and diffusional relaxation of the grain boundary (Jackson et al. 2014) or dislocation-enabled deformation of individual grains (e.g. Hansen et al. 2011; Hansen et al. 2012ab); dislocation climb (e.g. Goetze and Kohlstedt 1973); and dislocation glide (e.g. Evans and Goetze 1979; Katayama and Karato 2008).

Dislocations play a particularly important role in the deformation of olivine under low temperature or moderate to high stress conditions, such as in the mantle wedge above a subducting slab. The strain rate in this creep regime is controlled by the rate of kink-pair nucleation, which depends on the elasticity of the crystal and the intrinsic lattice friction of the glide plane. This latter property is quantified by the Peierls stress, σ_p, the critical stress required to initiate free glide of a dislocation at 0 K. Defect chemistry can therefore exert an important influence if immobile impurities segregate strongly to dislocation cores and inhibit glide creep by pinning dislocations, a phenomenon called solute drag (Cottrell and Bilby 1949).

Olivine is a plastically anisotropic mineral, and develops a measurable lattice preferred orientation (LPO) when deformed in the dislocation glide-controlled creep regime (e.g. Nicolas and Christensen 1987; Mainprice 2007; Long and Silver 2009; Long and Becker 2010). The dominant slip system for dislocation creep at low pressure is [100](010). Pressure changes the preferred dominant slip system of olivine, and much of the variation in seismic wave anisotropy in the upper mantle is explicable in terms of this pressure-induced transition (Mainprice et al. 2005; Ohuchi et al. 2011; Raterron et al. 2016). At high pressure, the dominant slip system is [001](010), as this slip system hardens less in response to increasing pressure than the [100](010) slip system (Raterron et al. 2011; Hilairet et al. 2012).

Experimental studies have reported Peierls stresses for olivine, ranging widely from as little as 3.8 GPa (Idrissi et al. 2016) to ~15 GPa (Demouchy et al. 2013), although typical values are in the range 5-10 GPa (e.g. Evans and Goetze 1979; Kranjc et al. 2016; Proietti et al. 2016). The Peierls stress measured in these studies represents a weighted average of the Peierls stresses of the individual slip systems that contribute to the total strain. While σ_p has not been measured experimentally for any individual slip system in olivine, this information gap has been partially filled using atomic scale modeling. Mahendran et al. (2017) directly calculated σ_p for [001] and [100] screw dislocations gliding on several crystallographic planes. Consistent with experimental observations, they found that [100](010) glide is easier than [001](010) glide in forsterite, with Peierls stresses of 3.1 and 7.2 GPa, respectively, within the range of Peierls stresses reported from experiments.

Hydrogen, probably incorporated into the olivine lattice by protonation of cation vacancies (e.g. Martin and Donnay 1972; Bai and Kohlstedt 1993; Kohlstedt et al. 1996; Lemaire et al. 2004), can influence the rheology of olivine under conditions of low-temperature (<1273 K) and high-stress, reducing σ_p to 1.6-2.9 GPa (Katayama and Karato 2008). Similarly, the incorporation of water as the "titanoclinohumite" defect, consisting of charge-coupled $\{Ti_M\}^{\cdot\cdot}$ and $\{2H_{Si}\}''$ defects apparently results in a systematic increase in strain rate (Berry et al. 2005; Faul et al. 2016).

Protonated cation vacancies also change the preferred slip system in olivine. Ohuchi et al. (2012) investigated the effect of increasing water content on the dominant slip system, and observed that the [001](010) slip was preferred over [100](010) slip at moderate water contents, with the transition occurring at ~650 ppm H/Si. Natural olivine crystals in subduction zone-derived peridotites show this B-type fabric (Mizukami et al. 2004), and 'wet' olivine fabrics have also been found in some peridotites sourced from the deep upper mantle (Katayama et al. 2005). Such a change in preferred slip system may explain the existence of trench-parallel orientation of 'fast' shear-wave polarizations in mantle wedges above subduction zones (Margheriti et al. 1996; Smith et al. 2001), which has previously been attributed to trench-parallel flow. A water-induced change of deformation fabric implies that protonated vacancies have a differential effect on the critical resolved shear stresses (CRSS) of the dominant slip systems, whether by stabilizing dislocation kinks or reducing the Peierls stress.

Atomic-scale calculations show that the energy required to create an Mg vacancy is considerably less than that required to create a Si vacancy (Wright and Catlow 1994; Brodholt 1997). Similarly, protonated Mg vacancies have lower energies than protonated Si vacancies (Walker et al. 2007). In the Earth's upper mantle, which is $MgSiO_3$-saturated, M-site vacancies in olivine can thus be expected to be many orders of magnitude more abundant than protonated Si vacancies. The predominance of M site vacancies in mantle olivine could be reinforced in oxidized regions of the mantle, as the oxidation of Fe^{2+} to Fe^{3+} may be accompanied by the creation of M-site vacancies to maintain charge neutrality. The two mechanisms for creating mobile M-site vacancies may co-exist, particularly in mantle wedges above subduction zones, which are oxidized by fluid transfer from the subducting slab (Kelley and Cottrell 2009). High oxygen fugacity has been shown to enhance seismic attenuation in olivine (Cline et al. 2018). The similarly high oxygen fugacities present in the earlier deformation experiments of Faul et al. (2016), produced by the platinum sleeve used to wrap the specimen (Faul et al. 2017), may

indicate that oxidizing conditions may indicate that ferric-iron associated vacancies may have a comparable effect to water on the rheology of olivine.

In this study we use computational simulations to investigate the possibility that cation vacancies may be able to lubricate dislocation glide in forsterite by reducing the Peierls stress σ_p., providing a mechanism by which point defects may influence the rheology of this important mantle mineral in the glide-controlled creep regime. Core structures and Peierls stresses are calculated for important slip systems in forsterite using a semi-discrete Peierls-Nabarro (PN; Peierls 1940; Nabarro 1947) model. In the PN model, a dislocation is represented as a discrete array of partial dislocations distributed on the glide plane, with the balance between repulsive elastic forces and inelastic restoring forces determining the shape of the dislocation. The inelastic component of the dislocation energy is parametrized here using atomistic calculations of generalized stacking fault (GSF; Christian and Vítek 1970) energies on olivine slip planes, using empirical interatomic potentials to model interactions between ions. PN modeling has been used to investigate glide lubrication by interstitial hydrogen atoms (Lu et al. 2001) and vacant lattice sites (Lu and Kaxiras 2002) in fcc Al, and $\{2H_{Mg}\}^X$ defects in MgO (Skelton and Walker 2018). We consider only cation vacancies on the M1 and M2 sub-lattices, represented using Kröger-Vink notation (Kröger and Vink 1956) as $\{V_{M1}\}''$ as $\{V_{M2}\}''$, such as may be created in mantle olivine by oxidation of Fe^{2+} to Fe^{3+} at fO_2 or through incorporation of water under hydrous conditions.

2. Methods

In the PN model, a dislocations with finite core-width is represented as continuous (e.g. Joós et al. 1994) or discrete (e.g. Bulatov and Kaxiras 1997) distribution of dislocation density along the glide plane. Here we use an implementation of the discrete approach previously used for modeling lubrication of dislocation glide in MgO (Skelton and Walker 2018). The total energy of such a finite distribution of dislocations at a distance R from the dislocation line is

$$E_{TOT}(R) = E_{INTERNAL} + E_{LONG-RANGED}(R) \quad (1)$$

where $E_{LONG\text{-}RANGED}$ is the elastic strain energy of the dislocation contained within radius R and $E_{INTERNAL}$ is the internal energy of the dislocation distribution. This can be further decomposed as

$$E_{INTERNAL} = E_{ELASTIC} + E_{MISFIT} \quad (2)$$

where $E_{ELASTIC}$ is the energy due to elastic interactions between the components of the dislocation density and E_{MISFIT} is the inelastic energy due to the lattice discontinuity across the glide plane. If **u**(x) is the disregistry across the slip plane and $\rho(x) = d\,u_i(x)/dx$ is the associated dislocation density distribution, then the elastic energy of the dislocation is the work required to insert this disregistry into an infinite elastic medium:

$$E_{ELASTIC}[\rho(x)] = -K \iint \rho(x')\rho(x) \ln|x - x'|\, dx'\, dx \quad , \quad (3)$$

where K is the elastic energy pre-factor, derived from the dislocation geometry and the elastic constants, which are here calculated directly from the analytical derivatives of the total cell energy. In the absence of a restoring force, the repelling elastic force between components of the dislocation density distribution would cause the dislocation to have an infinitely wide core, with ρ zero everywhere. In real crystals, it is the energy penalty associated with introducing misfit on either side of the slip plane that provides this opposing force, and constrains dislocations to have finite width. For a given disregistry profile **u**(x), the inelastic energy is

$$E_{MISFIT} = \sum_n \gamma\left(u(na_p)\right) a_p \quad , \quad (4)$$

where a_p is the spacing between adjacent atomic planes and the function γ(**u**) (called the γ-line in 1D) gives the energy required to displace one half of a crystal by **u** (Christian and Vítek 1970). The equilibrium dislocation core structure is calculated by minimizing equation (2), under the constraint that the integral of the disregistry **u** equals the Burgers vector.

The evolution of the disregistry profile under the action of an applied stress σ is computed by adding $E_{WORK} = -\sigma \int u(x)dx$ to the total internal energy (equation 2) of the dislocation and minimizing the energy functional as before. At the Peierls stress, σ_p, the energy barrier inhibiting free translation of the dislocation disappears, allowing it to glide without resistance. This is equivalent to searching for the stress σ at which the total energy function has no energy minimum, so that σ_p corresponds to the minimum stress for which the energy minimization step fails (Bulatov and Kaxiras 1997).

The γ-surface energy used to calculate the inelastic energy of a dislocation density distribution is constructed from generalized stacking fault (GSF) energies obtained from atomistic calculations. In an atomistic simulation, a GSF is inserted by cutting a simulation cell with the appropriate orientation, and displacing one half with respect to the other by **u**, then allowing the atomic coordinates to relax to a local minimum energy configuration. For materials without rigid units, such as simple oxides, atomic positions are typically constrained to relax normal to the fault plane. However, olivine contains SiO_4 polyhedra, which accommodate shear strain primarily through rotation rather than deformation. To replicate this, in our simulations oxygen atoms have been permitted to relax freely while Mg and Si atoms can only move normal to the stacking fault plane. In all GSF calculations described here, a 15 Å thick vacuum layer was used to minimize interactions between the GSF and its periodic images. To ensure that the boundary conditions of the relaxation calculation match the bulk material, the coordinates of all atoms within 5 Å of the vacuum layer were held fixed. Calculated GSF energies depend on the thickness of the slab atoms used in the simulation. For stacking faults on (010), a slab thickness of 8*b*, where *b* is the length of the [010] lattice vector, was found to be sufficient to converge the [100](010) and [001](010) γ-line maxima to < 5 meV/Å^2.

In this study, owing to the large number of atoms in the simulation cells, atomic scale interactions are modeled using empirical interatomic potentials. These potentials are taken from a widely used potential

158 model, which was parameterized by fitting to experimental data (Sanders et al. 1984; Lewis and Catlow
159 1985), and reproduces the physical properties of forsterite reasonably well (Price et al. 1987). This
160 potential, labeled THB1, has been widely used to model point and extended defects in forsterite,
161 including Mg point defects (Wright and Catlow 1994), surface structures and energetics (de Leeuw et
162 al. 2000), and screw dislocation core structures and energies (Walker et al. 2005). The THB1 model
163 uses formal charges for the Mg^{2+} and Si^{4+} cations, while the polarizable oxygen anion is modeled as a
164 positively charged core coupled by a harmonic potential to a negatively-charged massless shell (Dick
165 and Overhauser 1958). Each cation-anion pair interacts through a Buckingham potential, while the
166 rigidity of the $(SiO_4)^{4-}$ tetrahedron is replicated using a short-ranged three-body harmonic potential. All
167 atomistic calculations are performed using the molecular mechanics software GULP (Gale 1997; Gale
168 and Rohl 2003).

169 The two defect species considered in this study, $\{V_{M1}\}''$ and $\{V_{M2}\}''$, are charged, and inserting them
170 into a simulation cell gives it a net charge. This is compensated for by applying a charge-neutralizing
171 background. Creating a vacancy in the simulation cell is simple, and involves removing from the
172 simulation cell a single atom of the desired type located a specified distance from the stacking fault
173 plane. The slab thicknesses used to calculate GSF energies in the absence of Mg vacancies are
174 sufficiently great to also ensure convergence of GSF energies with point defects present at the stacking
175 fault plane. To minimize interactions between point defects and their periodic images, simulations are
176 conducted by inserting a single Mg vacancy at the slip plane of a simulation cell with cross-section
177 2*a*x2*c*, which corresponds to a concentration of 0.125 defects/site at the stacking fault plane for both
178 the M1 and M2 sub-lattices. While this would represent an unrealistically high defect concentration in
179 the bulk lattice, the strain magnitude close to a dislocation core is substantial, so that the energy of an
180 Mg vacancy on a core site may be considerably lower than in the bulk, and the defect concentration

correspondingly greater. In the case of MgO, fully atomistic calculations of Mg vacancy segregation to 1/2<110>{110}edge dislocations give binding energy of up to 1.7 eV (Zhang et al. 2010).

3. Results

3.1 GSF energies in point defect free forsterite

In materials with complex lattices, like olivine, there may be several inequivalent planes on which slip can occur. We find that the lowest energy (010) stacking fault plane is located at z = 0.25 (or, equivalently, z = 0.75), intersecting the sheet of $M2O_6$ octahedra (Fig. 1a). The THB1 potential model has previously been validated by Mahendran et al. (2017) at 0 GPa, who compared [100](010) and [001](010) γ-lines calculated with the interatomic potential with the earlier DFT calculations by Durinck et al. (2005). Although GSF energies calculated with THB1 are qualitatively consistent with the DFT calculations, the energies calculated with the interatomic potential are somewhat higher, particularly for displacement along [001](010). Indeed, the magnitude of the difference may actually be understated, as Durinck et al. (2005) used atomic slabs only a single unit cell thick along the stacking fault normal, so that their *ab initio* computed GSF energies are unlikely to be fully converged with respect to slab thickness.

The difference between GSF energies obtained in *ab initio* and force field calculations may be due to the use of formal charges in the THB1 model. The introduction of a GSF into a simulation cell often brings ions at or near the stacking fault plane into close proximity with ions of like charge, so that partially ionic models should in general predict lower energies than those that use formal charges. The ionicity ζ of forsterite is calculated to be < 1 from refinements of electron density distributions obtained using theoretical calculations (Liu et al. 2009) and synchrotron x-ray diffraction (Kirfel et al. 2005). It is thus unsurprising that Durinck et al. (2005) find lower GSF energies than calculations that use the THB1 potential.

In our calculations, we find that in point defect-free forsterite the maximum energy along the [100](010) γ-line, which is the energy of a 1/2[100](010) GSF, increases monotonically with pressure from 0.140 eV/Å^2 at 0 GPa to 0.203 eV/Å^2 at 10 GPa (Fig. 2). By comparison, the energy of the 1/2[001](010) GSF, which is the [001](010) γ-line maximum, decreases modestly over the same pressure range, from 0.163 eV/Å^2 at 0 GPa to 0.142 eV/Å^2 at 10 GPa. This contrasts with DFT calculations (Durinck et al. 2005), which predict a pressure-independent [001](010) γ-line maximum energy, although this is likely a consequence of the different simulation parameters, including simulation cell size and relaxation constraints. While, at ambient pressure, the energy of the [100](010) γ-line maximum is lower than that of the [001](010) γ-line maximum, the qualitatively different responses of the two γ-lines to applied pressure mean that the [001](010) γ-line maximum is of lower energy above ~3 GPa. The higher GSF energies reported here are partly due to the stricter relaxation constraints, particularly for Mg atoms, which were allowed to relax freely in previous studies (Durinck et al. 2005; Mahendran et al. 2017) but are here constrained to relax normal to the stacking fault plane.

3.2 Influence of Mg vacancies on GSF energies

In the mantle, where olivine coexists with (Mg,Fe)SiO_3 pyroxene, Mg vacancies are expected to be more abundant than Si vacancies. In the bulk lattice, M1 vacancies have lower energies than M2 vacancies, and are thus more abundant (Brodholt 1997). Any change in the GSF energy will depend on the interaction between the Mg vacancy and the stacking fault, which can be expected to vary between the two sites. Considering first slip in the [100] direction, we find that the energy of the 1/2[100](010) GSF with a $\{V_{M1}\}''$ defect adsorbed to the stacking fault plane is 0.132 eV/Å^2 at 0 GPa, 5.7% lower than the value computed without point defects. The 1/2[100](010) GSF energy increases with pressure (Fig. 3), reaching 0.198 eV/Å^2 at 10 GPa, 2.5% less than the point defect-free value. $\{V_{M2}\}''$ defects have a more substantial impact on the calculated 1/2[100](010) GSF energy, reducing it to 0.121 eV/Å^2

at 0 GPa, 13.6% lower than the point defect-free value. Pressure decreases the relative reduction of the 1/2[100](010) GSF energy with adsorption of $\{V_{M2}\}''$; its value at 10 GPa (0.184 eV/Å^2) corresponds to a reduction of only 9.5%.

The 1/2[001](010) GSF energy calculated with a $\{V_{M1}\}''$ defect at the fault plane is 0.168 eV/Å^2 at ambient pressure, decreasing to 0.145 eV/Å^2 at 10 GPa. Comparing these with the values reported above for point defect-free case, we see that M1 vacancies do not lubricate [001](010) slip, and may actually inhibit it. In contrast, $\{V_{M2}\}''$ defects reduce the 1/2[001](010) GSF energy to 0.127 eV/Å^2 at 0 GPa, a decrease of -22.1%. At 10 GPa, the energy of this GSF is 0.101 eV/Å^2, corresponding to a -28.9% change in the GSF energy relative to the point defect-free GSF case. Overall, (010) stacking fault energies are reduced much more by the presence of M2 than M1 vacancies, unsurprising given that the fault plane intersects the sheet of $M2O_6$ octahedra. The lubrication effect is greatest for [001](010) γ-line energies, as the minimum distance between M2 sites across the fault plane is 2.61 Å (at the γ-line maximum), compared with 3.89 Å for the [100](010) γ-line. As the $\{V_{M2}\}''$ defect interacts more strongly than the $\{V_{M1}\}''$ defect with both 1/2[100](010) and [001](010) stacking faults, $\{V_{M2}\}''$ defects can be expected to be relatively more abundant near the dislocation core than in the bulk lattice.

The markedly different sensitivities of the [100](010) and [001](010) γ-lines to adsorption of $\{V_{M1}\}''$ versus $\{V_{M2}\}''$ defects to the stacking fault are a direct consequence of the location of the slip plane in the unit cell. As the lowest energy slip plane lies across the center of the sheet of $M2O_6$ octahedra that is parallel to the (010) plane, it does not intersect $M1O_6$ octahedra or SiO_4 tetrahedra (Fig. 1a), so that the creation of M1 vacancies cannot contribute to the total number of vacant lattice sites at the slip plane. Nevertheless, $\{V_{M1}\}''$ defects do still reduce the energy of the [100](010) γ-line, although [001](010) γ-line energies are essentially unchanged. This is because displacement of the upper half the simulation cell by 1/2[100] brings M2 and Si sites on opposite sites of the stacking plane into close proximity. Relaxing the atom in the M2 site away from the stacking fault reduces the energy of the

slab, which is easier when a void has been created above the M2 site by the insertion of a $\{V_{M1}\}''$ defect. At 0 GPa, this increases the relaxed M2-Si distance from 2.939 Å to 3.021 Å. Furthermore, a sub-periodic modulation of the M1 site coordinates is introduced, as the Mg atoms in the layer of M1 sites closest to the GSF stacking fault are displaced ~0.2 Å along the fault plane normal. The sign of the displacement vector alternates along [001]. For the olivine crystal structure, [001](010) slip does not cause cations to approach as closely as does [100](010) slip, and there is thus less potential for vacant cation sites away from the slip plane to reduce GSF energies by accommodating relaxation away from the stacking fault.

3.3 Peierls stresses of dislocations in point defect-free forsterite

Core structures and Peierls stresses for edge and screw dislocations in forsterite were calculated using the PN model (equation 2), with the inelastic energy parameterized using the γ-lines calculated in the previous section. At 0 GPa, the Peierls stress calculated for the [100](010) edge dislocation in the point defect-free crystal is 2.4 GPa, ~25% greater than the value computed by Durinck et al. (2007) using a DFT-parameterized continuous PN model. The Peierls stress increases with pressure (Fig. 4), reaching 6.3 GPa at 10 GPa, much higher than the corresponding value of 2.2 GPa calculated by Durinck et al. The pressure derivative of the Peierls stress is thus $d\sigma_p/dP = 0.39$. For the [001](010) edge dislocation, σ_p is calculated to be 3.4 GPa at ambient pressure, decreasing with increasing pressure to 1.4 GPa at 10 GPa, in qualitative agreement with DFT-parameterized PN calculations by Durinck et al. (2007). This gives a pressure derivative for the Peierls stress of $d\sigma_p/dP = -0.19$. The disagreement between this calculation and that of Durinck et al. may be partially attributed to the present use of a discrete PN model, in contrast to the continuous formulation employed by Durinck et al. However, the principal disagreement concerns the pressure dependence of the γ-line energies. Whereas in this study the [001](010) γ-line maximum decreases with pressure, the γ-line previously calculated is nearly pressure

independent (Durinck et al. 2005; Durinck et al. 2007). The cores of [100](010) and [001](010) edge dislocations are undissociated across the entire pressure range 0-10 GPa, consistent with previous PN calculations (Durinck et al. 2007).

A screw dislocation can glide on any lattice plane containing the dislocation line vector ξ. Each glide plane has a different structure and a correspondingly different lattice resistance, giving rise to preferred glide planes. Here, we calculate the Peierls stress for [100] and [001] glide on (010), corresponding to the screw dislocations that enable deformation of the [100](010) and [001](010) slip systems. The Peierls stress for glide of [100] on the (010) plane at ambient pressure (Fig. 5) is 6.8 GPa, comparable with the 6.3 GPa predicted by DFT-parametrized PN calculations (Durinck et al. 2007). However, we calculate $d\sigma_p/dP$ = 0.47, slightly greater than the pressure derivative of $d\sigma_p/dP$ = 0.39 calculated by Durinck et al. (2007). This is somewhat lower than the pressure derivative $d\sigma_p/dP$ ~0.67 measured in high-stress deformation experiments for the average Peierls stress, which is presumably controlled by the easy [100](010) slip system (Proietti et al. 2016).

The [001] screw dislocation glides on the (010) plane with a Peierls stress σ_p = 5.4 GPa at 0 GPa pressure (Fig. 5), comparable to values calculated in previous theoretical studies, which range between 3.1 GPa (Durinck et al. 2007) and 7.2 GPa (Mahendran et al. 2017). As was found for the [001](010) edge dislocation, pressure enhances glide on this slip system by reducing its Peierls stress, with $d\sigma_p/dP$ = -0.21. Fully atomistic calculations show that the static [001] screw dislocation core has a labile non-planar structure and that the effect of applied stress is to transform into a high core energy-low Peierls stress planar configuration (Carrez et al. 2008). The critical stress for dislocation glide is thus the stress required to activate the locking-unlocking mechanism for this slip system (Mahendran et al. 2017). This locking-unlocking mechanism cannot be modeled within the PN formalism, and the σ_p reported in this study is for the glissile (i.e. unlocked) dislocation core gliding on the median plane of the $M2O_6$ sheet.

3.4 Effect of vacancies on the Peierls stress

For [100](010) edge dislocations, the adsorption of a $\{V_{M1}\}''$ defect to the stacking fault plane reduces Peierls stress by -16% at ambient pressure, to 2.0 GPa. The pressure dependence of σ_p is not significantly changed by the presence of the defect as $d\sigma_p/dP$ = 0.37, compared with 0.39 calculated above for the point defect-free dislocation, and at 10 GPa σ_p = 5.7 GPa. The effect of the $\{V_{M2}\}''$ defect is more substantial, and for this defect σ_p = 1.2 GPa at ambient pressure, slightly more than half the Peierls stress calculated for a dislocation without adsorbed vacancies. Moreover, unlike the $\{V_{M1}\}''$ defect, $\{V_{M2}\}''$ defects reduce the pressure sensitivity of this slip system, as $d\sigma_p/dP$ = 0.31. At 10 GPa, σ_p = 4.3 GPa, -31% lower than the value calculated above.

As can be seen in Fig. 4, the [001](010) edge dislocation responds quite differently from [100](010) edge dislocation to the presence of Mg vacancies. The adsorption of a $\{V_{M1}\}''$ defect to the stacking fault plane increases [001](010) γ-line energies, leading to considerably higher Peierls stresses for the [001](010) edge dislocation. At ambient pressure, σ_p = 3.7 GPa, nearly 10% greater than the Peierls stress without point defects. The Peierls stress decreases with pressure at a rate $d\sigma_p/dP$ = -0.10. Compared with the $d\sigma_p/dP$ calculated for this dislocation without adsorbed point defects, $\{V_{M1}\}''$ reduces the pressure sensitivity of [001](010) slip by almost a factor of 2. Unlike $\{V_{M1}\}''$ defects, $\{V_{M2}\}''$ defects reduce the [001](010) γ-line energy. Correspondingly, as can be seen in Fig. 4c, the Peierls stress of the [001](010) edge dislocation is considerably reduced by $\{V_{M2}\}''$, to 1.6 GPa at 0 GPa applied pressure, decreasing to only 150 MPa at 10 GPa, giving $d\sigma_p/dP$ = -0.14. Due to the relative softness of this slip system, the relative Peierls stress reduction actually increases with pressure, from -52% at 0 GPa to -90% at 10 GPa.

For [100](010) screw dislocations (Fig. 5), the presence of Mg vacancies at the glide plane reduces the Peierls stress. If the Mg vacancy is located on an M2 site, σ_p is calculated to be 6.1 GPa, 10.2% lower than in point defect-free forsterite, and increases with pressure to 10.7 GPa at 10 GPa. The pressure sensitivity of the [100] screw dislocation is unaffected by $\{V_{M1}\}''$ defects as $d\sigma_p/dP$ = 0.46, nearly identical to the value found previously for this dislocation in the absence of adsorbed vacancies. For an Mg vacancy located on an M1 site close to (but not on) the slip plane, calculated values for σ_p at these pressures are comparable, 6.3 GPa and 10.8 GPa at 0 and 10 GPa, respectively, as is the pressure derivative $d\sigma_p/dP$, which is 0.45.

The Peierls stresses of [001] screw dislocations gliding on (010) are similarly reduced by the presence of M2 vacancies at the slip plane, to 3.0 GPa at ambient pressure and 0.8 GPa at 10 GPa (Fig. 5). The pressure derivative $d\sigma_p/dP$ = -0.21, identical to the value above for point defect-free forsterite. Unlike the [100](010) screw dislocation, the relative Peierls stress reduction induced by the presence of M2 vacancies actually increases with pressure, from -44% at ambient pressure to -75% at 10 GPa. However, just as in the case of [001](010) edge dislocations, glide of [001] screw dislocations on (010) is modestly inhibited by the presence of M1 vacancies. At ambient pressure, σ_p = 5.7 GPa, decreasing to 4.3 GPa at 10 GPa pressure. The magnitude of $d\sigma_p/dP$ is reduced by ~1/3, to -0.14, relative to the point defect-free value.

4. Discussion

In vacancy-free forsterite, the ratio $\sigma_{p,[100]}/\sigma_{p,[001]}$ increases with P for both the edge and screw components of both slip systems. For edge dislocations, $\sigma_{p,[100]}/\sigma_{p,[001]}$ varies from 0.71 at ambient pressure, to 4.4 at 10 GPa (Fig. 6a). The addition of $\{V_{M1}\}''$ vacancies changes this ratio, decreasing it to 0.54 at ambient pressure and reducing the pressure sensitivity so that, at 10 GPa, it is just 2.16. In contrast, $\{V_{M2}\}''$ defects increase the ratio, to 0.77 at 0 GPa and 28.51 at 10 GPa. In each case, the ratio

342 $\sigma_{p,[100]}/\sigma_{p,[001]} = 1$ corresponds to the pressure at which [100](010) glide becomes harder than [001](010)
343 glide. This occurs at 1.5 GPa with no point defects present, increasing to 3.6 GPa when $\{V_{M1}\}''$ defects
344 are adsorbed to the stacking fault and decreases to 0.7 GPa upon adsorption of $\{V_{M2}\}''$ defects to the
345 stacking fault plane. In the case of screw dislocations, $\sigma_{p,[100]}/\sigma_{p,[001]}$ is strictly > 1. However, $\{V_{M1}\}''$
346 defects reduce it from 1.26 to 1.09 at ambient pressure, and from 3.49 to 2.50 at 10 GPa. The $\{V_{M2}\}''$
347 defect has the reverse effect on the two slip systems, increasing $\sigma_{p,[100]}/\sigma_{p,[001]}$ to 2.06 at ambient pressure
348 and 13.10 and 10 GPa. From this, we conclude that, while $\{V_{M1}\}''$ defects cause the relative activities
349 of the two slip systems to converge at constant *P*, $\{V_{M2}\}''$ defects enhance slip on [001](010).

350 As qualitatively predicted by our models, experimental studies have reported a pressure-induced
351 change in the deformation fabric of anhydrous olivine, caused by a change of the preferred slip system
352 from [100](010) to [001](010) (Couvy et al. 2004; Raterron et al. 2016). This transition may be
353 observable in seismological models for the Earth's upper mantle. The LPO of Fe-bearing Fo_{90} olivine
354 suggests a change from dominant [100](010) to [001](010) slip at ~3 GPa, which corresponds to a
355 mantle depth of approximately 70-80 km (Jung et al. 2009). At 0 GPa, the [100](010) edge dislocation
356 has the lowest Peierls stress and so should be the dominant slip system during glide deformation.
357 However, because pressure is calculated to suppress the activity of this slip system, the Peierls stress of
358 the [001](010) edge dislocation is lower at high pressure. The *P*-σ_p curves of the two slip systems in
359 point defect-free forsterite intersect at 1.5 GPa (Fig. 4a), slightly lower than the pressures reported in
360 experiments.

361 Deformation experiments produce different olivine textures under dry and wet conditions. One
362 plausible reason for this is that hydrated vacancies lubricate [001](010) glide more than [100](010)
363 glide (Katayama et al. 2004), leading to the development of the flow normal B-type fabric associated
364 with the mantle wedge. Ohuchi et al. (2012) have found that the transition between the two fabrics
365 occurs at ~650 ppm H/Si. Consistent with this, we find that the Peierls stresses of [100](010) edge and

screw dislocations are reduced less by the presence of M-site vacancies than [001](010) edge and screw dislocations. Realistic vacancy-related defect concentrations are insufficient to change the weakest slip system at ambient pressure. However, the differential effect on the Peierls stresses of the [100](010) and [001](010) edge dislocations is enough to reduce the pressure at which the Peierls stresses of the two slip systems cross over. When the inelastic restoring force is parametrized using the γ-lines calculated with vacancies adsorbed to the slip plane, $P_{\text{cross-over}}$ decreases from 1.5 GPa to 0.7 GPa. Higher defect concentrations at the dislocation core will cause the slip system cross-over to be displaced to even lower pressures. Similarly, differences between concentrations of vacancy-related defects at the glide planes of the two slip systems will displace the cross-over pressure. Increasing the concentration $\{V_{M2}\}''$ defects adsorbed to the [100](010) dislocation or decreasing the concentration of defects adsorbed to the [001](010) dislocation will reduce $P_{cross\text{-}over}$. Changing either of the concentrations in the opposite direction increases $P_{cross\text{-}over}$.

The calculated influence of vacancy-related defects on the Peierls stress of olivine may be of significance for development of LPO during deformation. It has also been suggested that a distinct LPO may form in olivine when it is deformed via diffusion creep (Miyazaki et al. 2013). Similarly, a transition to a grain boundary sliding deformation mechanism may explain the presence of the B-type deformation fabric, rather than water-induced changes to the relative strengths of olivine slip systems. However, as these calculations show, the adsorption of vacancies, and by implication vacancy-related defects, is sufficient to induce a change in the deformation fabric of olivine similar to that observed by Katayama and Karato (2008) under hydrous conditions. In tomographic images of shear wave anisotropy, this might show up as a reduction of the depth at which the deformation fabric changes from A-type (i.e. [100](010)) to B-type (i.e. [001](010)). Alternatively, if water is present only at shallow depths, the shear wave anisotropy may match the B-type fabric at shallow depths, transitioning to the A-type deformation fabric as the modal abundance of water decreases. The B-type deformation

fabric then re-emerges at high pressure as the relative activity of the [001](010) slip system increases. These conclusions carry over to the dislocation-accommodated grain-boundary sliding regime. This deformation mechanism leads to the development of a pronounced LPO that relates to the slip system accommodating grain boundary sliding (Hansen et al. 2011; Hansen et al. 2012ab), which will be altered by the presence of hydrous vacancies.

Incorporation of water is not the only mechanism by which vacancies can be generated in olivine minerals. Trivalent cations such as Al^{3+}, Sc^{3+} and Fe^{3+} can substitute for Mg^{2+} (or Fe^{2+}) in the olivine lattice, charge-balanced either the replacement of Si^{4+} by a trivalent cation or, more commonly, the creation of M-site vacancies (Colson et al. 1989). The latter substitution mechanism can be written as

$$3\cdot\left(M_M^{2+}\right)^X + M_2^{3+}O_3 \rightleftharpoons 2\cdot\left(M_M^{3+}\right)^{\cdot} + \left(V_M\right)'' + 3\cdot M^{2+}O \quad , \tag{5}$$

where M^{2+} is typically Mg^{2+} or, in iron-bearing olivine, Fe^{2+} and M^{3+} is the substituting trivalent cation. These vacancies can influence the mechanical properties of olivine, for instance by enhancing seismic attenuation due to grain boundary mechanisms (Cline et al. 2018). The solubility of common trivalent elements in olivine is sufficiently high that vacancies created by the substitution reaction (5) can greatly outnumber intrinsic vacancies, such as those associated with Schottky defects (van Orman et al. 2009). In $(Mg,Fe)_2SiO_4$, M-site vacancies are produced by oxidation of iron from Fe^{2+} to Fe^{3+}, and at high fO_2 $\{Fe^{3+}_M\}^{\cdot}$ and $\{V_M\}''$ are the most abundant defects (Stocker 1978). These defects may be unassociated at high temperature and pressure, as they are in the common oxide (Mg,Fe)O (Otsuka et al. 2010), and we expect such vacancies to alter the Peierls stress of dislocations in olivine.

5. Conclusions

In this study, we used atomistic calculations of generalized stacking fault energies in forsterite, the Mg end-member of olivine, to parameterize Peierls-Nabarro models of pure edge and screw dislocation. To probe the possible influence of vacancy-related defects on the Peierls stress, energies were calculated

for GSFs in point defect-free forsterite, and with $\{V_{M1}\}''$ and $\{V_{M2}\}''$ defects segregated to lattice sites in close proximity to the stacking fault plane. It was found that vacancies are capable of reducing γ-line energies and, correspondingly, Peierls stresses for many of the major slip systems in olivine. However, the magnitude of this decrease depends strongly on both the slip system and the site on which the vacancy is located. $\{V_{M2}\}''$ defects at lattice sites adjacent to the glide plane have the greatest effect on the Peierls stress of both slip systems, while the magnitude of the σ_p reduction is greatest for the [001](010) slip system. In the case of edge dislocations, this reduces the pressure at which the hardening of [100](010) glide cause [001](010) to become the dominant slip system.

Cation vacancies in olivine are associated with intrinsic defect mechanisms (Schottky and Frenkel defects). However, in natural olivine, vacancy concentrations are, in most cases, probably controlled by extrinsic defect mechanisms, such as the creation of protonated vacancies in hydrated systems, the oxidation of Fe^{2+} to Fe^{3+}, or the charge-balanced substitution of heterovalent impurities, such Al^{3+} or Cr^{3+}. Each of these mechanisms will be operative in at least some regions of the Earth's upper mantle. Hydration and oxidation are especially relevant in mantle wedges above subduction zones. There, concentrations of vacancy related defects are likely to be elevated, due to the combination of oxidizing conditions and the availability of liquid water from dehydrating phases in the subducting slab. Our models suggest that these intrinsic point defects can reduce the Peierls stress of dislocations in olivine in mantle wedges, potentially linking crystal chemistry to the observed variations in seismic anisotropy in these regions.

Acknowledgements

AMW is grateful for support from the UK Natural Environment Research Council (NE/K008803/1 and NE/M000044/1). RS is supported by an Australian Government Research Training Program (RTP) Scholarship. Calculations were performed on the Terrawulf cluster, a computational facility supported through the AuScope initiative. AuScope Ltd is funded under the National Collaborative Research

Infrastructure Strategy (NCRIS), an Australian Commonwealth Government Programme. This work used the ARCHER UK National Supercomputing Service (http://www.archer.ac.uk). The authors would like to thank Ian Jackson and Joshua Muir for their helpful comments on the manuscript during its preparation.

References

Bai, Q., Kohlstedt, D.L., 1993. Effects of chemical environment on the solubility and incorporation mechanism for hydrogen in olivine. Phys Chem Minerals 19, 460–471. https://doi.org/10.1007/BF00203186

Berry, A.J., Hermann, J., O'Neill, H.S.C., Foran, G.J., 2005. Fingerprinting the water site in mantle olivine. Geology 33, 869–872. https://doi.org/10.1130/G21759.1

Braithwaite, J.S., Sushko, P.V., Wright, K., Catlow, C.R.A., 2002. Hydrogen defects in Forsterite: A test case for the embedded cluster method. The Journal of Chemical Physics 116, 2628–2635. https://doi.org/10.1063/1.1433465

Brodholt, J., 1997. Ab initio calculations on point defects in forsterite (Mg2SiO4) and implications for diffusion and creep. American Mineralogist 82, 1049–1053. https://doi.org/10.2138/am-1997-11-1201

Christian, J.W., Vítek, V., 1970. Dislocations and stacking faults. Rep. Prog. Phys. 33, 307. https://doi.org/10.1088/0034-4885/33/1/307

Bulatov, V.V., Kaxiras, E., 1997. Semidiscrete Variational Peierls Framework for Dislocation Core Properties. Phys. Rev. Lett. 78, 4221–4224. https://doi.org/10.1103/PhysRevLett.78.4221

Carrez, P., Walker, A.M., Metsue, A., Cordier, P., 2008. Evidence from numerical modelling for 3D spreading of [001] screw dislocations in Mg2SiO4 forsterite. Philosophical Magazine 88, 2477–2485. https://doi.org/10.1080/14786430802363804

Cline II, C.J., Faul, U.H., David, E.C., Berry, A.J., Jackson, I., 2018. Redox-influenced seismic properties of upper-mantle olivine. Nature 555, 355–358. https://doi.org/10.1038/nature25764

Colson, R.O., McKay, G.A., Taylor, L.A., 1989. Charge balancing of trivalent trace elements in olivine and low-Ca pyroxene: A test using experimental partitioning data. Geochimica et Cosmochimica Acta 53, 643–648. https://doi.org/10.1016/0016-7037(89)90007-0

Cottrell, A.H., Bilby, B.A., 1949. Dislocation Theory of Yielding and Strain Ageing of Iron. Proc. Phys. Soc. A 62, 49. https://doi.org/10.1088/0370-1298/62/1/308

Couvy, H., Frost, D.J., Heidelbach, F., Nyilas, K., Ungár, T., Mackwell, S., Cordier, P., 2004. Shear deformation experiments of forsterite at 11 GPa - 1400°C in the multianvil apparatus. European Journal of Mineralogy 16, 877–889. https://doi.org/10.1127/0935-1221/2004/0016-0877

Demouchy, S., Tommasi, A., Boffa Ballaran, T., Cordier, P., 2013. Low strength of Earth's uppermost mantle inferred from tri-axial deformation experiments on dry olivine crystals. Physics of the Earth and Planetary Interiors 220, 37–49. https://doi.org/10.1016/j.pepi.2013.04.008

Dick, B.G., Overhauser, A.W., 1958. Theory of the Dielectric Constants of Alkali Halide Crystals. Phys. Rev. 112, 90–103. https://doi.org/10.1103/PhysRev.112.90

Durinck, J., Legris, A., Cordier, P., 2005. Pressure sensitivity of olivine slip systems: first-principle calculations of generalised stacking faults. Phys Chem Minerals 32, 646–654. https://doi.org/10.1007/s00269-005-0041-2

Durinck, J., Carrez, P., Cordier, P., 2007. Application of the Peierls-Nabarro model to dislocations in forsterite. European Journal of Mineralogy 19, 631–639. https://doi.org/10.1127/0935-1221/2007/0019-1757

Evans, B., Goetze, C., 1979. The temperature variation of hardness of olivine and its implication for polycrystalline yield stress. J. Geophys. Res. 84, 5505–5524. https://doi.org/10.1029/JB084iB10p05505

Faul, U.H., Cline II, C.J., David, E.C., Berry, A.J., Jackson, I., 2016. Titanium-hydroxyl defect-controlled rheology of the Earth's upper mantle. Earth and Planetary Science Letters 452, 227–237. https://doi.org/10.1016/j.epsl.2016.07.016

Faul, U.H., Ii, C.J.C., Berry, A., Jackson, I., Garapić, G., 2017. Constraints on oxygen fugacity within metal capsules. Phys Chem Minerals 1–13. https://doi.org/10.1007/s00269-017-0937-7

Gale, J.D., 1997. GULP: A computer program for the symmetry-adapted simulation of solids. J. Chem. Soc., Faraday Trans. 93, 629–637. https://doi.org/10.1039/A606455H

Gale, J.D., Rohl, A.L., 2003. The General Utility Lattice Program (GULP). Molecular Simulation 29, 291–341. https://doi.org/10.1080/0892702031000104887

Goetze, C., Kohlstedt, D.L., 1973. Laboratory study of dislocation climb and diffusion in olivine. J. Geophys. Res. 78, 5961–5971. https://doi.org/10.1029/JB078i026p05961

Hansen, L.N., Zimmerman, M.E., Kohlstedt, D.L., 2011. Grain boundary sliding in San Carlos olivine: Flow law parameters and crystallographic-preferred orientation. J. Geophys. Res. 116, B08201. https://doi.org/10.1029/2011JB008220

Hansen, L.N., Zimmerman, M.E., Kohlstedt, D.L., 2012a. The influence of microstructure on deformation of olivine in the grain-boundary sliding regime. J. Geophys. Res. 117, B09201. https://doi.org/10.1029/2012JB009305

Hansen, L.N., Zimmerman, M.E., Kohlstedt, D.L., 2012b. Laboratory measurements of the viscous anisotropy of olivine aggregates. Nature 492, 415. https://doi.org/10.1038/nature11671

Hilairet, N., Wang, Y., Sanehira, T., Merkel, S., Mei, S., 2012. Deformation of olivine under mantle conditions: An in situ high-pressure, high-temperature study using monochromatic synchrotron radiation. J. Geophys. Res. 117, B01203. https://doi.org/10.1029/2011JB008498

Idrissi, H., Bollinger, C., Boioli, F., Schryvers, D., Cordier, P., 2016. Low-temperature plasticity of olivine revisited with in situ TEM nanomechanical testing. Science Advances 2, e1501671. https://doi.org/10.1126/sciadv.1501671

Jackson, I., Faul, U.H., Skelton, R., 2014. Elastically accommodated grain-boundary sliding: New insights from experiment and modeling. Physics of the Earth and Planetary Interiors, High-Pressure Research in Earth Science: Crust, Mantle, and Core 228, 203–210. https://doi.org/10.1016/j.pepi.2013.11.014

Joós, B., Ren, Q., Duesbery, M.S., 1994. Peierls-Nabarro model of dislocations in silicon with generalized stacking-fault restoring forces. Phys. Rev. B 50, 5890–5898. https://doi.org/10.1103/PhysRevB.50.5890

Jung, H., Mo, W., Green, H.W., 2009. Upper mantle seismic anisotropy resulting from pressure-induced slip transition inolivine. Nature Geosci 2, 73–77. https://doi.org/10.1038/ngeo389

Katayama, I., Karato, S., 2008. Low-temperature, high-stress deformation of olivine under water-saturated conditions. Physics of the Earth and Planetary Interiors 168, 125–133. https://doi.org/10.1016/j.pepi.2008.05.019

Katayama, I., Jung, H., Karato, S., 2004. New type of olivine fabric from deformation experiments at modest water content and low stress. Geology 32, 1045–1048. https://doi.org/10.1130/G20805.1

Katayama, I., Karato, S., Brandon, M., 2005. Evidence of high water content in the deep upper mantle inferred from deformation microstructures. Geology 33, 613–616. https://doi.org/10.1130/G21332.1

Kelley, K.A., Cottrell, E., 2009. Water and the Oxidation State of Subduction Zone Magmas. Science 325, 605–607. https://doi.org/10.1126/science.1174156

Kirfel, A., Lippmann, T., Blaha, P., Schwarz, K., Cox, D.F., Rosso, K.M., Gibbs, G.V., 2005. Electron density distribution and bond critical point properties for forsterite, Mg2 SiO4, determined with synchrotron single crystal X-ray diffraction data. Phys Chem Minerals 32, 301–313. https://doi.org/10.1007/s00269-005-0468-5

Kohlstedt, D.L., Keppler, H., Rubie, D.C., 1996. Solubility of water in the α, β and γ phases of (Mg,Fe)2SiO4. Contrib Mineral Petrol 123, 345–357. https://doi.org/10.1007/s004100050161

Kranjc, K., Rouse, Z., Flores, K.M., Skemer, P., 2016. Low-temperature plastic rheology of olivine determined by nanoindentation. Geophys. Res. Lett. 43, 2015GL065837. https://doi.org/10.1002/2015GL065837

Kröger, F.A., Vink, H.J., 1956. Relations between the Concentrations of Imperfections in Crystalline Solids. Solid State Physics 3, 307–435. https://doi.org/10.1016/S0081-1947(08)60135-6

de Leeuw, N.H., Parker, S.C., Catlow, C.R.A., Price, G.D., 2000. Modelling the effect of water on the surface structure and stability of forsterite. Phys Chem Min 27, 332–341. https://doi.org/10.1007/s002690050262

Lemaire, C., Kohn, S.C., Brooker, R.A., 2004. The effect of silica activity on the incorporation mechanisms of water in synthetic forsterite: a polarised infrared spectroscopic study. Contrib Mineral Petrol 147, 48–57. https://doi.org/10.1007/s00410-003-0539-x

Lewis, G.V., Catlow, C.R.A., 1985. Potential models for ionic oxides. J. Phys. C: Solid State Phys. 18, 1149. https://doi.org/10.1088/0022-3719/18/6/010

Liu, L., Du, J., Zhao, J., Liu, H., Gao, H., Chen, Y., 2009. Elastic properties of hydrous forsterites under high pressure: First-principle calculations. Physics of the Earth and Planetary Interiors 176, 89–97. https://doi.org/10.1016/j.pepi.2009.04.004

Long, M.D., Becker, T.W., 2010. Mantle dynamics and seismic anisotropy. Earth and Planetary Science Letters 297, 341–354. https://doi.org/10.1016/j.epsl.2010.06.036

Long, M.D., Silver, P.G., 2009. Shear Wave Splitting and Mantle Anisotropy: Measurements, Interpretations, and New Directions. Surv Geophys 30, 407–461. https://doi.org/10.1007/s10712-009-9075-1

Lu, G., Kaxiras, E., 2002. Can Vacancies Lubricate Dislocation Motion in Aluminum? Phys. Rev. Lett. 89, 105501. https://doi.org/10.1103/PhysRevLett.89.105501

Lu, G., Zhang, Q., Kioussis, N., Kaxiras, E., 2001. Hydrogen-Enhanced Local Plasticity in Aluminum: An Ab Initio Study. Phys. Rev. Lett. 87, 095501. https://doi.org/10.1103/PhysRevLett.87.095501

Mahendran, S., Carrez, P., Groh, S., Cordier, P., 2017. Dislocation modelling in Mg 2 SiO 4 forsterite: an atomic-scale study based on the THB1 potential. Modelling Simul. Mater. Sci. Eng. 25, 054002. https://doi.org/10.1088/1361-651X/aa6efa

Mainprice, D., 2007. Seismic Anisotropy of the Deep Earth from a Mineral and Rock Physics Perspective, in: Treatise of Geophysics, Vol.2. Elsevier, pp. 437–491.

Mainprice, D., Tommasi, A., Couvy, H., Cordier, P., Frost, D.J., 2005. Pressure sensitivity of olivine slip systems and seismic anisotropy of Earth's upper mantle. Nature 433, 731. https://doi.org/10.1038/nature03266

564 Margheriti, L., Nostro, C., Cocco, M., Amato, A., 1996. Seismic anisotropy beneath the Northern
565 Apennines (Italy) and its tectonic implications. Geophys. Res. Lett. 23, 2721–2724.
566 https://doi.org/10.1029/96GL02519

567 Martin, R.F., Donnay, G., 1972. Hydroxyl in the mantle. American Mineralogist 57, 554–570.

568 Miyazaki, T., Sueyoshi, K., Hiraga, T., 2013. Olivine crystals align during diffusion creep of Earth/'s
569 upper mantle. Nature 502, 321–326. https://doi.org/10.1038/nature12570

570 Mizukami, T., Wallis, S.R., Yamamoto, J., 2004. Natural examples of olivine lattice preferred
571 orientation patterns with a flow-normal a-axis maximum. Nature 427, 432–436.
572 https://doi.org/10.1038/nature02179

573 Mei, S., Kohlstedt, D.L., 2000. Influence of water on plastic deformation of olivine aggregates: 1.
574 Diffusion creep regime. J. Geophys. Res. 105, 21457–21469. https://doi.org/10.1029/2000JB900179

575 Nabarro, F.R.N., 1947. Dislocations in a simple cubic lattice. Proc. Phys. Soc. 59, 256.
576 https://doi.org/10.1088/0959-5309/59/2/309

577 Nicolas, A., Christensen, N.I., 1987. Formation of Anisotropy in Upper Mantle Peridotites - A Review,
578 in: Fuchs, K., Froidevaux, C. (Eds.), Composition, Structure and Dynamics of the Lithosphere-
579 Asthenosphere System. American Geophysical Union, pp. 111–123.
580 https://doi.org/10.1029/GD016p0111

581 Ohuchi, T., Kawazoe, T., Nishihara, Y., Nishiyama, N., Irifune, T., 2011. High pressure and temperature
582 fabric transitions in olivine and variations in upper mantle seismic anisotropy. Earth and Planetary
583 Science Letters 304, 55–63. https://doi.org/10.1016/j.epsl.2011.01.015

584 Ohuchi, T., Kawazoe, T., Nishihara, Y., Irifune, T., 2012. Change of olivine a-axis alignment induced
585 by water: Origin of seismic anisotropy in subduction zones. Earth and Planetary Science Letters 317–
586 318, 111–119. https://doi.org/10.1016/j.epsl.2011.11.022

587 van Orman, J.A., Fei, Y., Hauri, E.H., Wang, J., 2003. Diffusion in MgO at high pressures: Constraints
588 on deformation mechanisms and chemical transport at the core-mantle boundary. Geophys. Res. Lett.
589 30, 1056. https://doi.org/10.1029/2002GL016343

590 Otsuka, K., McCammon, C.A., Karato, S., 2010. Tetrahedral occupancy of ferric iron in (Mg,Fe)O:
591 Implications for point defects in the Earth's lower mantle. Physics of the Earth and Planetary Interiors,
592 Transport properties of the lower mantle 180, 179–188. https://doi.org/10.1016/j.pepi.2009.10.005

593 Peierls, R., 1940. The size of a dislocation. Proc. Phys. Soc. 52, 34. https://doi.org/10.1088/0959-
594 5309/52/1/305

595 Price, G.D., Parker, S.C., Leslie, M., 1987. The lattice dynamics and thermodynamics of the Mg2SiO4
596 polymorphs. Phys Chem Minerals 15, 181–190. https://doi.org/10.1007/BF00308782

Proietti, A., Bystricky, M., Guignard, J., Béjina, F., Crichton, W., 2016. Effect of pressure on the strength of olivine at room temperature. Physics of the Earth and Planetary Interiors 259, 34–44. https://doi.org/10.1016/j.pepi.2016.08.004

Raterron, P., Chen, J., Geenen, T., Girard, J., 2011. Pressure effect on forsterite dislocation slip systems: Implications for upper-mantle LPO and low viscosity zone. Physics of the Earth and Planetary Interiors 188, 26–36. https://doi.org/10.1016/j.pepi.2011.06.009

Raterron, P., Chen, J., Li, L., Weidner, D., Cordier, P., 2016. Pressure-induced slip-system transition in forsterite: Single-crystal rheological properties at mantle pressure and temperature. American Mineralogist 92, 1436–1445. https://doi.org/10.2138/am.2007.2474

Sanders, M.J., Leslie, M., Catlow, C.R.A., 1984. Interatomic potentials for SiO2. J. Chem. Soc., Chem. Commun. 1271–1273. https://doi.org/10.1039/C39840001271

Skelton, R., Walker, A.M., 2018. Lubrication of dislocation glide in MgO by hydrous defects. Phys Chem Minerals 1–14. https://doi.org/10.1007/s00269-018-0957-y

Smith, G.P., Wiens, D.A., Fischer, K.M., Dorman, L.M., Webb, S.C., Hildebrand, J.A., 2001. A Complex Pattern of Mantle Flow in the Lau Backarc. Science 292, 713–716. https://doi.org/10.1126/science.1058763

Stocker, R.L., 1978. Influence of oxygen pressure on defect concentrations in olivine with a fixed cationic ratio. Physics of the Earth and Planetary Interiors 17, 118–129. https://doi.org/10.1016/0031-9201(78)90053-5

Walker, A.M., Gale, J.D., Slater, B., Wright, K., 2005. Atomic scale modelling of the cores of dislocations in complex materials part 2: applications. Phys. Chem. Chem. Phys. 7, 3235–3242. https://doi.org/10.1039/B505716G

Walker, A.M., Hermann, J., Berry, A.J., O'Neill, H.S.C., 2007. Three water sites in upper mantle olivine and the role of titanium in the water weakening mechanism. J. Geophys. Res. 112, B05211. https://doi.org/10.1029/2006JB004620

Wright, K., Catlow, C.R.A., 1994. A computer simulation study of (OH) defects in olivine. Phys Chem Minerals 20, 515–518. https://doi.org/10.1007/BF00203222

Zhang, F., Walker, A.M., Wright, K., Gale, J.D., 2010. Defects and dislocations in MgO: atomic scale models of impurity segregation and fast pipe diffusion. J. Mater. Chem. 20, 10445–10451. https://doi.org/10.1039/C0JM01550D

Figure captions

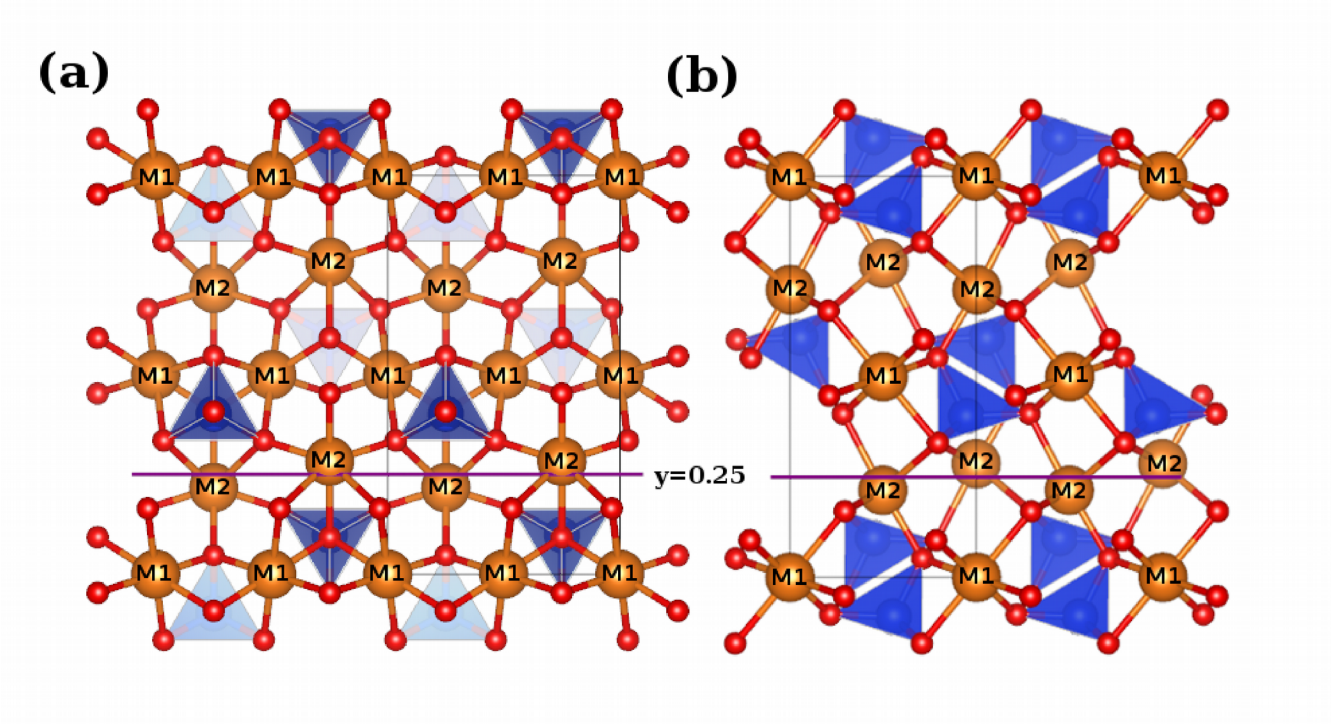

628 **Fig. 1** The olivine unit cell, viewed down the (a) [100] and (b) [001] cell directions, with the M1 and M2 sites
629 labeled. The easy glide plane for dislocations gliding on (010) is marked. Visualization produced using VESTA 3
630 (Momma and Izumi 2011).

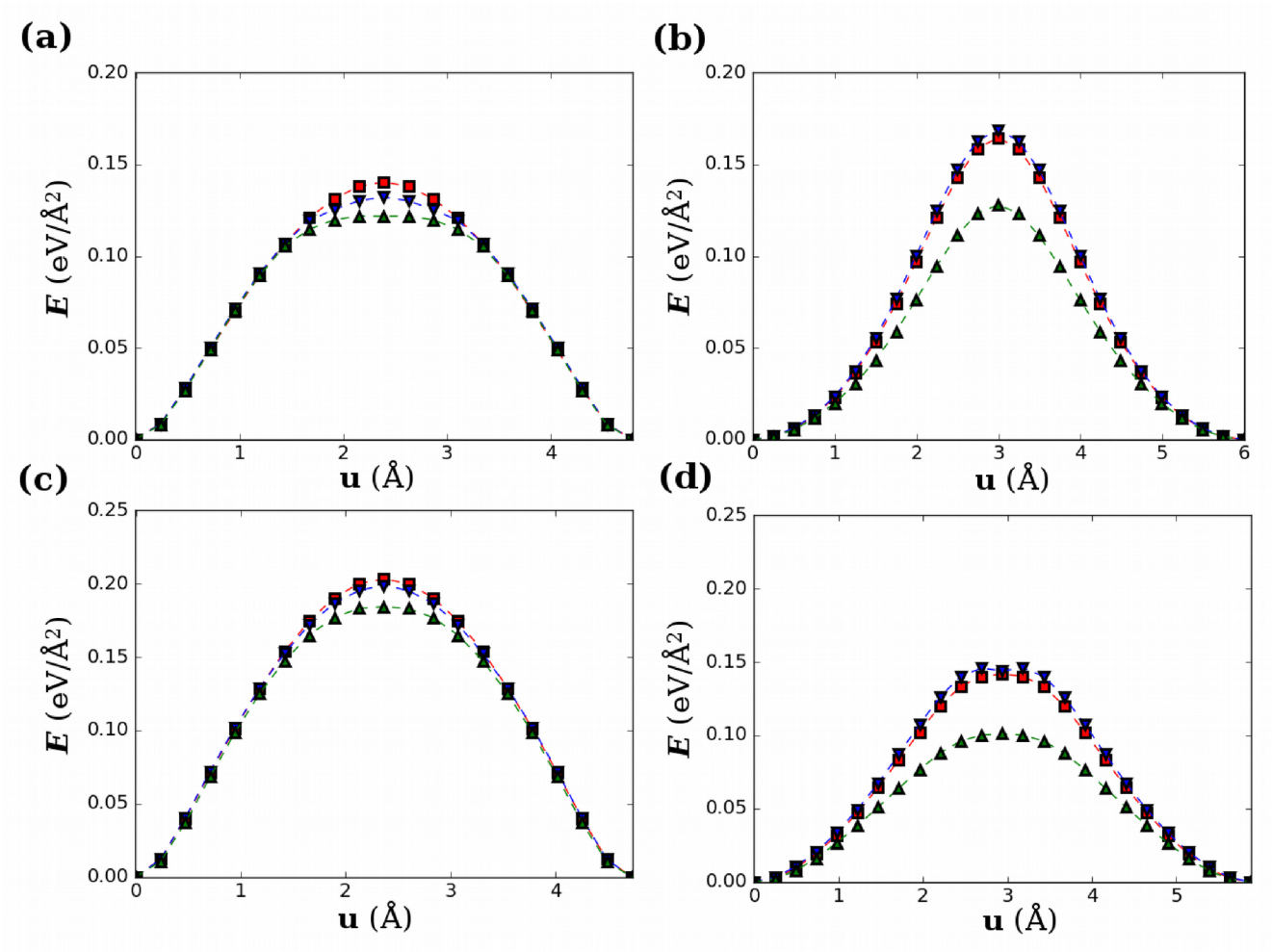

631 **Fig. 2** (a) [100](010) and (b) [001](010) γ-lines at 0 GPa. (c) [100](010) and (d) [001](010) γ-lines at 10 GPa.

632 Square, triangle, and inverted triangle symbols correspond to GSFs without point defects, with $\{V_{M2}\}''$ defects,

633 and with $\{V_{M1}\}''$ defects.

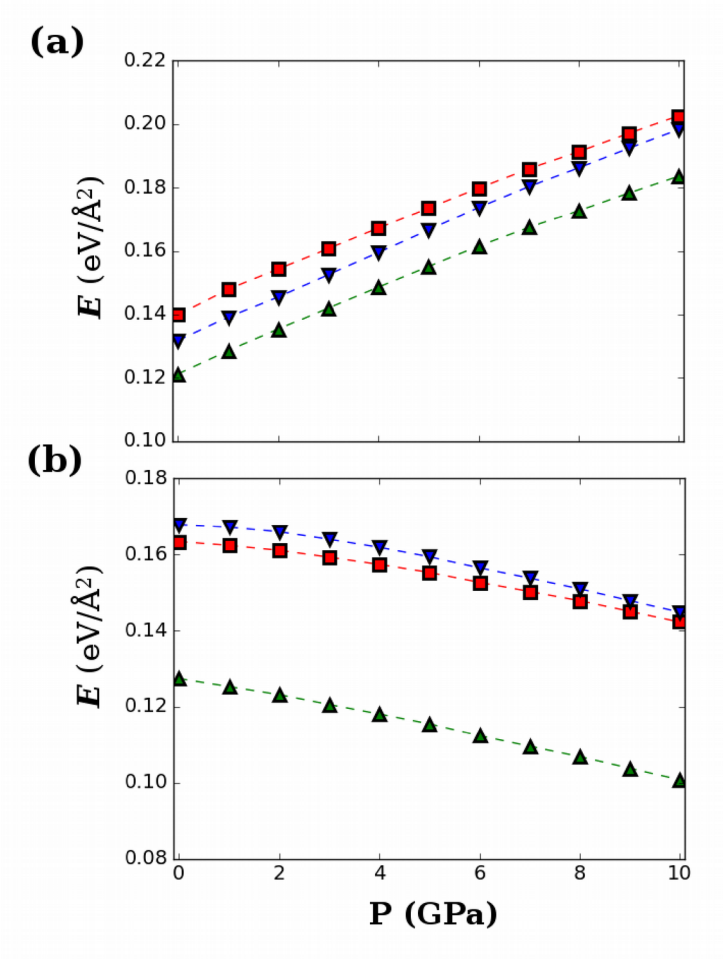

634 **Fig. 3** Maximum energies along the (a) [100](010) and (b) [001](010) γ-lines. Symbols have the same meaning

635 as in Fig. 2.

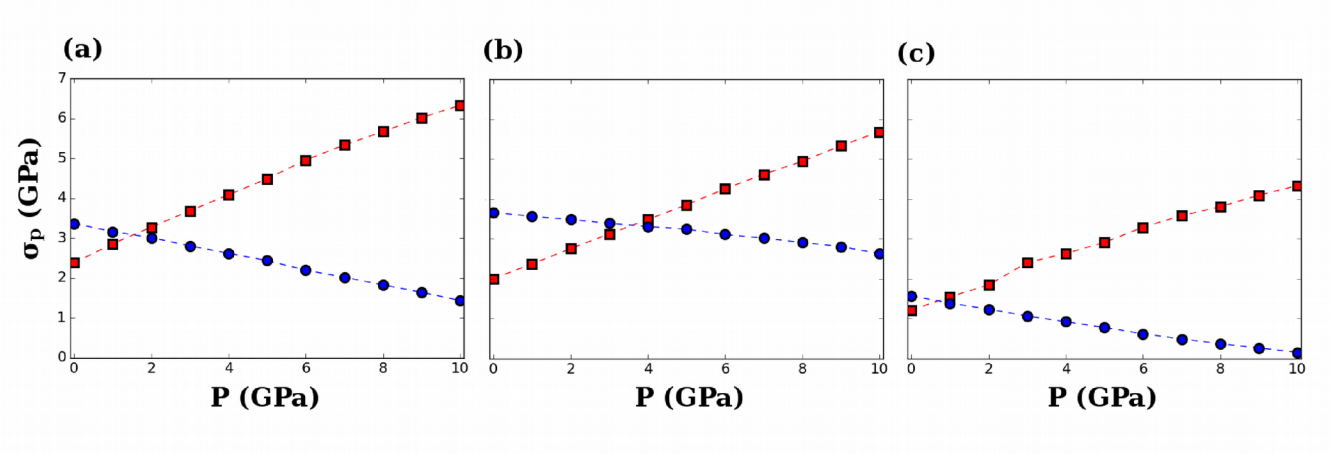

636 **Fig. 4** Pressure evolution of σ_p for (squares) [100](010) and (circles) [001](010) edge dislocations with (a) no
637 point defects, (b) a $\{V_{M1}\}''$ defect, and (c) a $\{V_{M2}\}''$ defect at the glide plane. All Peierls stresses are plotted using
638 the same scale. Symbols have the same meaning as in Fig. 2.

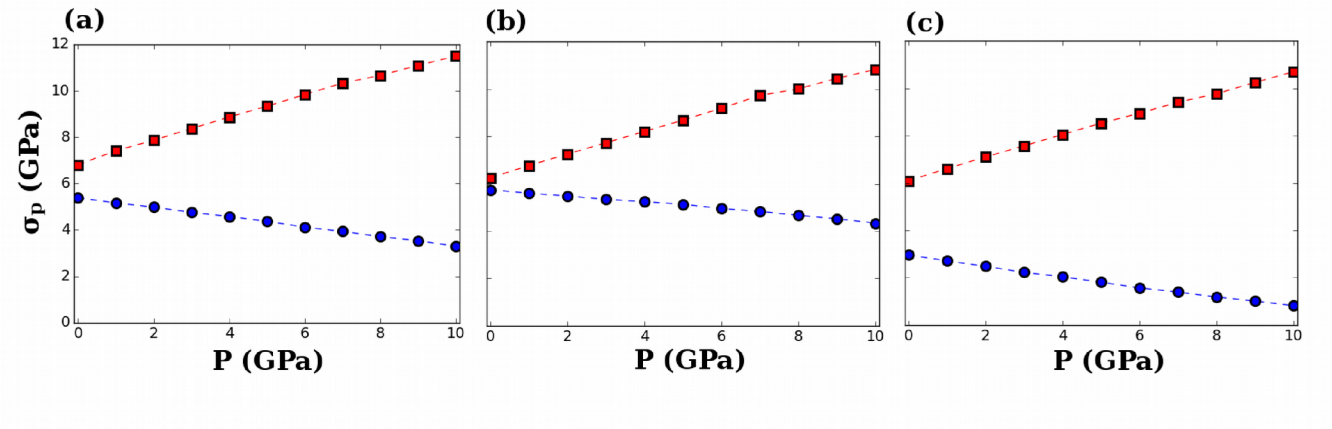

639 **Fig. 5** Pressure evolution of σ_p for (squares) [100](010) and (circles) [001](010) screw dislocations with (a) no
640 point defects, (b) a $\{V_{M1}\}''$ defect, and (c) a $\{V_{M2}\}''$ defect at the glide plane. All Peierls stresses are plotted using
641 the same scale.

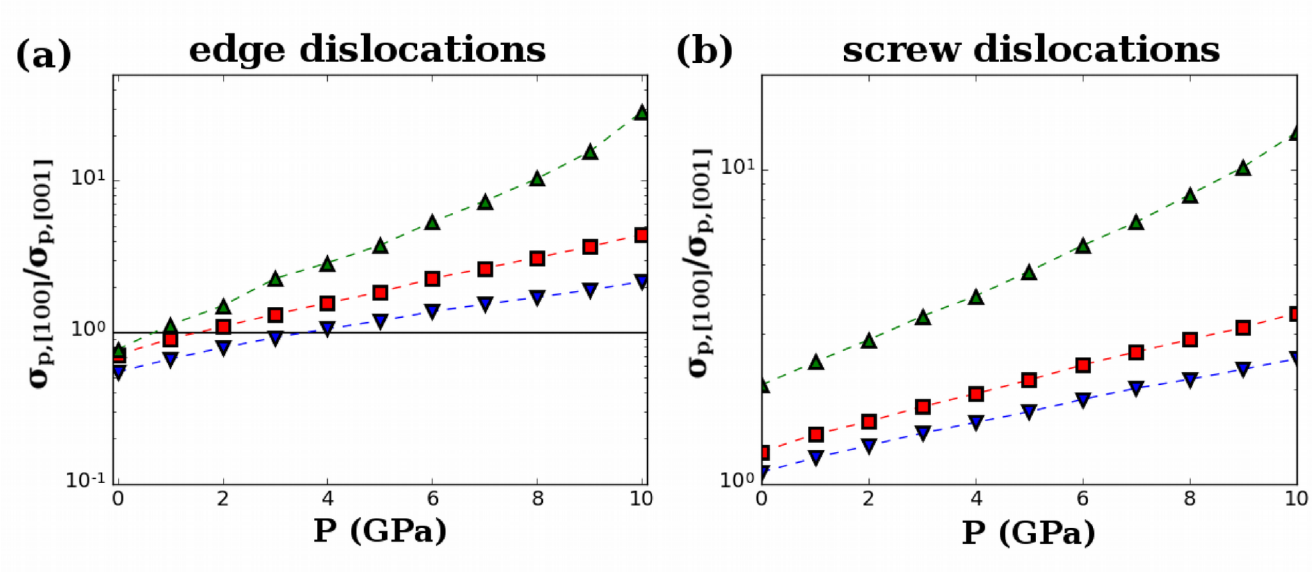

642 **Fig. 6** $\sigma_{p,[100]}/\sigma_{p,[001]}$ ratios for (a) edge, and (b) screw dislocations. Symbols have the same meaning as in Fig. 2.